submitted to *Geophys. J. Int.*

Acoustic full waveform inversion for 2-D ambient noise source imaging

Arjun Datta[1], Bharath Shekar[2], Pushp L. Kumar[1]

[1] *Department of Earth and Climate Science, Indian Institute of Science Education and Research, Pune, India*

[2] *Department of Earth Sciences, Indian Institute of Technology Bombay, Mumbai, India*

Accepted date. Received date; in original form date

SUMMARY

We present a method for estimating seismic ambient noise sources by acoustic full waveform inversion of interstation cross-correlations. The method is valid at local scales for laterally heterogeneous media, and ambient noise sources confined to the Earth's surface. Synthetic tests performed using an actual field array geometry, are used to illustrate three unique aspects of our work. First: the method is able to recover noise sources of arbitrary spatial distribution, both within and outside the receiver array, with high fidelity. This holds true for complex velocity models and does not require a good initial guess for inversion, thereby addressing an outstanding issue in the existing research literature. Second: we analyse the extent of biases in source inversion that arise due to inaccurate velocity models. Our findings indicate that source inversion using simplified (e.g. homogeneous) velocity models may work reliably when lateral variations in velocity structure are limited to 5 or 10% in magnitude, but is vitiated by strong variations of 20% or higher, wherein the effect of strong scattering and/or phase distortions become significant. Finally, our technique is implemented without the adjoint method, which is usually inextricably linked to full waveform inversion. Inversions are performed using source kernels computed for each receiver pair, and this approach is computationally tractable for real-world problems with small aperture seismic arrays.

Key words: Seismic noise; seismic interferometry; waveform inversion; inverse theory

1 INTRODUCTION

The study of the ambient seismic field, or seismic ambient noise as it is popularly known, is now firmly entrenched in mainstream seismological research. Ambient seismic sources can shed light on such natural phenomena as ocean wave coupling with the seafloor (e.g. Juretzek & Hadziioannou 2016), sediment transport in rivers (Tsai et al. 2012), glacier hydrology and dynamics (e.g. Aso et al. 2017; Labedz et al. 2022), tropical cyclones (e.g. Retailleau & Gualtieri 2019) and underground hydrothermal activity (e.g. Cros et al. 2011). On the other hand, seismologists are widely interested in using ambient noise as a tool for studying Earth structure, typically by applying interferometric techniques to extract meaningful signals from noise recordings (e.g. Shapiro & Campillo 2004). Even in this case, source information is essential because the spatial distribution of noise sources effectively determines whether inter-station Green's functions can be accurately recovered from noise cross-correlations (Roux et al. 2005; Snieder 2004). There is ample evidence for biases in structure estimation, arising from realistic distributions of ambient noise sources on Earth (e.g. Kimman & Trampert 2010; Yao & van der Hilst 2009). If one chooses instead to leverage the power of full waveform inversion (FWI), the assumption of Green's function retrieval is dropped and both sources and structure must be simultaneously estimated (Sager et al. 2018b; Zhou et al. 2022). Thus, regardless of one's particular interest in seismic ambient noise, the ability to determine the strength and locations of the noise sources is of vital importance.

Traditional, computationally cheap methods for locating ambient sources include beamforming (e.g. Gal et al. 2015; Gerstoft & Tanimoto 2007), matched-field processing (e.g. Cros et al. 2011) and backprojection (e.g. Liu et al. 2016) as well as cross-correlation based imaging (e.g. Ermert et al. 2016; Tian & Ritzwoller 2015). The last few years have witnessed the emergence of FWI methods, which seek to match observed noise cross-correlations with theoretically modelled ones, incorporating their finite frequency sensitivity to spatially distributed sources (Fichtner et al. 2017; Tromp et al. 2010). This paper focusses on FWI to recover noise source distribution with the assumption of a known structure model (Datta et al. 2019; Ermert et al. 2017, 2021; Igel et al. 2021; Xu et al. 2019, 2020). These 'source inversion' techniques are useful in their own right, and essential components in the toolkit for the larger problem of full waveform noise cross-correlation tomography (e.g. Sager et al. 2020).

FWI, by definition, entails wave-equation based forward modelling. However, different approximations to the seismic wave equation (e.g. acoustic vs. elastic) or different assumptions about the medium of propagation, lead to a family of methods achieving varying degrees of modelling rigour. From analytical modelling in homogeneous or laterally homogeneous media (Datta et al. 2019; Xu et al. 2019, 2020) to numerical simulations in spherically symmetric (Igel et al. 2021) or full 3-D Earth models (Ermert et al. 2017, 2021) at global scales, a variety of methods have been proposed. In this study, we present an approach using acoustic modelling in 2-D media that incorporates laterally heterogeneous structure information. Xu et al. (2020) used classic surface wave analysis on ambient noise data (Bensen et al. 2007) to estimate a uniform phase velocity required for forward modelling. With our approach, one can go a step further by using the 2-D phase or group velocity maps obtained from ambient noise surface wave tomography (Shapiro 2019).

Independent of our choice of modelling scheme, another highlight of this study, achieved by building on the work of Datta et al. (2019), is the ability to localize sources outside the sensor array. Previous non-global studies, deploying a range of strategies for data measurement and misfit definition, have had limited success in this regard. For example, Xu et al. (2019) reported that both traveltime and waveform inversion are only able to estimate rough source directions, rather than actual locations and shapes, when sources are outside the array. Ermert et al. (2020) demonstrated recovery of outside-array sources for a 1-D medium, but for a waveform-difference misfit function, which admittedly suffers from high sensitivity to velocity model inaccuracies. Their 'asymmetry misfit', discussed below, is robust with respect to velocity inaccuracies but offers poor resolution outside the sensor array. Against the backdrop of these challenges, our method recovers external source shapes and sizes fairly accurately, provided a moderate inter-sensor path density is available. It does not require a good initial source model, and can tolerate 2-D velocity model errors of up to 10%.

The two aforementioned features of our method — incorporation of 2-D structure, integrity of resolution outside the station array — lend themselves readily to a scrutiny of the source-structure trade-off in seismic interferometry (Fichtner 2014), which is not very well documented. Xu et al. (2019) reported the failure of source inversion in case of inaccurate structure models, but only for homogeneous halfspace models devoid of lateral variations. Other studies have argued that misfit functions defined using measurements of waveform asymmetry are very weakly sensitive to lateral structural variations (Igel et al. 2021; Sager et al. 2018a). These studies quantify cross-correlation waveform asymmetry via a logarithmic ratio of energies in the the causal and acausal branches. In our approach, we measure waveform energy on a single cross-correlation branch (rather than the ratio of energies on the two branches), and find that structure (velocity) information does impact source inversion.

In the following, we first present the methodology for forward and inverse modelling (Section 2), followed by synthetic tests (Section 3) which form the basis of our focussed Conclusions (Section 4) and a more general Discussion (Section 5).

2 CROSS-CORRELATION MODELLING AND INVERSION

Datta et al. (2019) introduced a method for estimating noise source directionality in a homogeneous medium. The limitation of estimating only directions was imposed by the choice of model parameterization, and the homogeneous medium assumption allowed for cross-correlations to be modelled analytically. In this study, we extend their method on both fronts. A similar but less restrictive model parameterization allows actual source locations and shapes to be estimated, and integration with a numerical solver eliminates the need to assume a homogeneous medium. However the choice of measurement, calculation of kernels and inversion strategy, remain essentially unchanged.

2.1 Forward modelling

The foundation of the method is a forward model for computing the cross-correlation $C(\mathbf{x}_\alpha, \mathbf{x}_\beta)$ between any pair of receivers α and β:

$$C(\mathbf{x}_\alpha, \mathbf{x}_\beta; \omega) = P(\omega) \int d^2\mathbf{x}\, G^*(\mathbf{x}_\alpha, \mathbf{x}; \omega) G(\mathbf{x}_\beta, \mathbf{x}; \omega) \sigma(\mathbf{x}), \tag{1}$$

where ω is angular frequency, P is the source power spectrum, G is the (scalar) Green function for the medium, σ is the source strength, and the position coordinate $\mathbf{x}$ is limited to a horizontal plane (approximating an area on the Earth's surface). The asterisk denotes complex conjugation. In case of elastic modelling, appropriate components of the elastodynamic Green tensor need to be used instead of the scalar G. Equation 1 follows from the formulation of Tromp et al. (2010), subject to the following assumptions (e.g. Malkoti et al. 2021; Xu et al. 2019):

(i) all ambient seismic sources are confined to the Earth's surface, so that the integral in (1) is a surface integral

(ii) all sources have the same spectral shape $P(\omega)$, so that the power spectral density (S) of noise sources can be separated into its positional and frequency contributions, i.e. $S(\mathbf{x}, \omega) = P(\omega)\sigma(\mathbf{x})$.

The frequency-domain expression (1) can be evaluated semi-analytically when closed form solutions for G are available — such as in a homogeneous (Datta et al. 2019) or 1-D (Malkoti et al. 2021) medium.

In anticipation of numerically solving the wave equation for heterogeneous media, we recast the expression for crosscorrelation in equation (1) in terms of the wavefields u:

$$C(\mathbf{x}_\alpha, \mathbf{x}_\beta; \omega) = \int d^2\mathbf{x}\, u^*(\mathbf{x}, \mathbf{x}_\alpha; \omega) u(\mathbf{x}, \mathbf{x}_\beta; \omega) \sigma(\mathbf{x}), \tag{2}$$

with $u(\mathbf{x}, \mathbf{x}_\alpha; \omega) = P(\omega)^{1/2} G(\mathbf{x}, \mathbf{x}_\alpha; \omega)$. Note that source-receiver reciprocity has also been invoked for computational efficiency, turning every receiver location into a source (e.g. Hanasoge 2014; Xu et al. 2019). The monochromatic wavefields in equation (2) can be computed in the frequency domain (e.g. Kumar et al. 2022). However, we use a time-domain finite difference solver implemented using "Devito" (Louboutin et al. 2019; Luporini et al. 2020), a Python package that can generate optimized codes based on symbolic input of governing equations using SymPy (Meurer et al. 2017). We use a uniform finite-difference stencil in Devito that is second-order in time and fourth-order in space. Equation (2) in the time domain is

$$C(\mathbf{x}_\alpha, \mathbf{x}_\beta; t) = \int d^2\mathbf{x} \int_{-\infty}^{\infty} d\tau \; u(\mathbf{x}, \mathbf{x}_\alpha; \tau) u(\mathbf{x}, \mathbf{x}_\beta; t+\tau)\, \sigma(\mathbf{x}). \tag{3}$$

We obtain $u(\mathbf{x}, \mathbf{x}_\alpha; \tau)$ as the solution to the acoustic wave equation with a source wavelet equal to the inverse Fourier transform of $P(\omega)^{1/2}$. Provided that the computed wavefields $u(\mathbf{x}, \mathbf{x}_\alpha)$ can be stored in memory, N numerical simulations are required to obtain all possible cross-correlations for an N-receiver array. In the inverse problem of estimating $\sigma(\mathbf{x})$, these N simulations, once performed at the start, are not required to be repeated every iteration, because the velocity model is held fixed.

2.2 Model parameterization

As in Datta et al. (2019), the model space is parameterized using a set of 2-D Gaussian basis functions, $B_j(\mathbf{x})$. In this study, we introduce a non-negative parameterization to ensure that the iterative optimization scheme (Section 2.3) does not lead to unphysical, negative values for $\sigma(\mathbf{x})$:

$$\sigma(\mathbf{x}) = \sum_j m_j^2 B_j(\mathbf{x}), \tag{4}$$

m_j being the basis function coefficients that are directly inverted for. We note that alternate means of enforcing positivity are available, such as in Xu et al. (2019). A second feature of our parameterization is that the basis functions are present uniformly throughout the domain, rather than merely in a ring surrounding the receiver array (Datta et al. 2019). The size and spacing of the Gaussian basis are user-controlled parameters, held fixed during inversion. The default specifications used in this study (Section 3 and Table 3.1), lead to a total of 625 basis functions, as shown in Figure 1.

2.3 Inversion Strategy

We follow the inversion strategy detailed in Datta et al. (2019, Appendix A), subject to minor changes necessitated by the model parameterization, equation (4). To summarize, we use a misfit

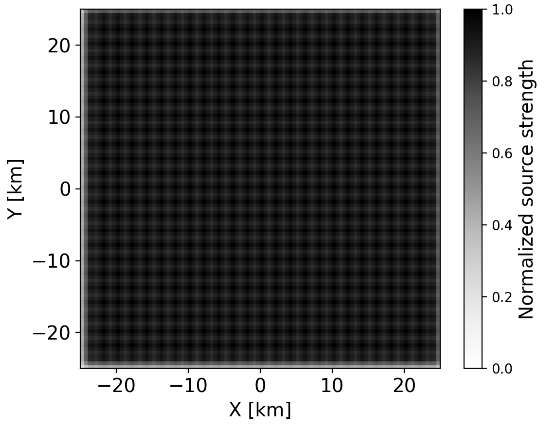

Figure 1. Source distribution obtained by setting $m_j = 1$ in equation (4).

function defined by Hanasoge (2013):

$$\chi = \frac{1}{2}\sum_i \left(\ln \frac{E_i^{obs}}{E_i^{syn}}\right)^2, \tag{5}$$

where the index i runs over receiver pair combinations, and E, the measurement, is the waveform energy in a time window of interest $w(t)$ on either the positive or negative cross-correlation branch:

$$E_i = \sqrt{\int w(t) C_i^2(t) dt} \tag{6}$$

When working with real data, one can define a measurement window aimed at encompassing the dominant signal arrivals on each correlation branch (Datta et al. 2019). However in this synthetic study, windowing is not necessary and we let $w(t)$ span the entire positive or negative correlation branch.

Local optimization techniques require the gradient of χ, or a misfit kernel K satisfying $\delta\chi = -\int K(\mathbf{x})\delta\sigma(\mathbf{x})d^2\mathbf{x}$. This misfit kernel is the sum of individual source kernels for each receiver pair (K_i), weighted by the corresponding misfit (Hanasoge 2013):

$$K = \sum_i \ln\left(\frac{E_i^{obs}}{E_i^{\mathrm{syn}}}\right) K_i(\mathbf{x}) \tag{7}$$

Using (4), we get the following expression for the gradient ($\mathbf{g}$) of χ:

$$g_j = \frac{\partial\chi}{\partial m_j} = -\int 2K(\mathbf{x}) m_j B_j(\mathbf{x})\, d^2\mathbf{x} \tag{8}$$

K, and therefore $\mathbf{g}$, can be obtained by either evaluating (7), which requires all the individual source kernels K_i, or by adjoint techniques, which build K from adjoint wavefields and 'event kernels' (Tromp et al. 2010), without access to the individual K_i. We use the former, non-adjoint approach. Using an analogy from earthquake traveltime tomography, this is akin to the difference between calculating individual banana doughnut kernels (e.g. Dahlen et al. 2000) or not (Tromp et al. 2005).

Our approach remains computationally feasible because numerical simulations are not required to obtain the K_i in every iteration, as explained in Section 2.1. Furthermore, we parallelise the implementation over the individual receivers. The advantage of this inversion strategy is that in addition to the gradient, it gives us access to the Jacobian through the individual kernels. Combining (7) and (8), the elements of our Jacobian matrix ($\mathbf{J}$) are:

$$J_{ij} = \int 2K_i(\mathbf{x}) m_j B_j(\mathbf{x}) \, d^2\mathbf{x} \tag{9}$$

The Jacobian can in turn be used to build an approximation to the Hessian operator, paving the way for optimization methods such as the Gauss-Newton method, which we use. For details of how this is done, and complete derivations of equations (8) and (9), the reader is referred to Appendix A of Datta et al. (2019). Here we wish to highlight two subtleties:

(i) Our least-squares inversion is regularized or damped in the usual way, by the L_2 norm of model misfit, weighted by a damping parameter determined by L-curve analysis (Hansen & O'Leary 1993). This corresponds to a diagonal model covariance matrix. Additional smoothing, which we do not use in this synthetic study, can be imposed through a banded model covariance matrix.

(ii) The entire workflow described in this section, from measurement to optimization, is executed separately for positive and negative cross-correlation branches. At the end of each iteration, the model update from the two sets of optimizations, is averaged to obtain the updated model.

3 SYNTHETIC TESTS

We conduct a series of synthetic tests using the field array geometry of Datta et al. (2019), which corresponded to an exploration seismic deployment by Shell. This choice is motivated by the relatively large number of receivers (289) in the array, which allows us to explore the effects of different array sizes and path densities, by randomly picking different subsets of receivers. We present results in this paper for two sub-array geometries, one with 20 and the other with 50 receivers (Figure 2, parts b and c, respectively). Synthetic tests with more than 50 receivers did not produce significantly different results.

Our default modelling domain size is 50 km $\times$ 50 km, and simulations are performed with $P(\omega)$ set to a Gaussian centred at 0.2 Hz, with a standard deviation of 0.05 Hz. Assuming a wavespeed of 2 km/s to define a homogeneous medium, we have a dominant wavelength (λ_0) of 10 km. The shortest wavelength is $\approx$ 5 km when velocity perturbations are introduced (Section 3.1), so we choose a conservative grid spacing of 0.5 km, which ensures a minimum of 10 grid points per wavelength in all cases. The size of the model basis functions (5 km across) is comparable to the shortest wavelength. Table 3.1 summarizes the various parameters used in our simulations.

We present results for two test source models, TSM-1 (Fig. 2d) and TSM-2 (Fig. 2g). In actual field scenarios, TSM-1 may represent, for example, roads situated close to or passing through, the receiver array. TSM-2 is more of a toy model, containing sources of varying strengths located entirely outside the array. The test models are built independently, without using the parameterization (4), which is reserved for the inverse problem.

For both test models, “observed data” are synthetically generated by forward modelling and adding noise to the resulting cross-correlation waveforms. We add Gaussian noise with a standard deviation equal to 10$\%$ of the average RMS value of all the computed crosscorrelations (e.g. Ermert et al. 2020). The frequency band of the noise (0.05-1 Hz) is kept wider than that of the power spectrum $P(\omega)$ used in the simulations ($\sim 0.05 - 0.35$ Hz).

For inversion, a quasi-uniform source distribution (Figure 1 and 2a) is used as a prior as well as the initial model. This initial model has very low amplitude compared to the test models, but it cannot be zero because of the logarithmic misfit function (5) used in the inversion. Finally, we note that inversions may be performed with either analytical or numerical modelling, because a homogeneous medium is assumed. For consistency with Section 3.1, we have presented results obtained with numerical modelling. The results with analytical Green functions were similar to those in Figure 2 and have not been shown.

Figure 2 shows that the inversion recovers true source locations and shapes fairly well, for both test models. As expected, results with 50 receivers are better than those with 20, but the improvement is modest, especially for sources lying outside the receiver array (TSM-2). The pixellated appearance of the inversion results as compared to the test models, is due to the parameterization (4) and the size of basis functions used (Table 3.1). In this way, our model parameterization dictates the resolution of the inverse problem, for a given frequency band and array geometry. For our chosen simulation parameters, we have verified with 'spike tests' that it is possible, in parts of the model domain, to accurately recover a source represented by a single basis function. A formal resolution analysis (e.g. Xu & Mikesell 2022), which would yield resolution as a function of spatial position, is beyond the scope of this paper.

Some examples of waveform fits involved in the inversions of Figure 2, are shown in Appendix A, where we address the question of how much noise our inverse method can tolerate. Reasonable inversion results, with only a marginal drop in quality, have been obtained with up to 50% added noise. However, for the sake of clarity in the next section, we use 10% noise amplitude as the default setting throughout the paper. Another question which arises at this point is with regard to the effect of distance — up to what distance from the array can sources be faithfully recovered by inversion? The tests of Figure 2 contain sources at a maximum distance of 25 km from the array centre. In Appendix B, we enlarge the domain to incorporate sources at larger distances, and find that far-away sources can be significantly distorted, as observed by Ermert et al. (2020). To put this limitation in perspective, it is important to remember that our method, in its current implementation, is unsuitable for distances over which Earth's sphericity becomes important.

In this paper we choose to focus on the question of how source inversions are impacted by unmodelled lateral heterogeneities in velocity structure. For the sake of uniformity, we adhere to the simulation parameters of Table 3.1, so that inversion results can be benchmarked against those of Figure 2.

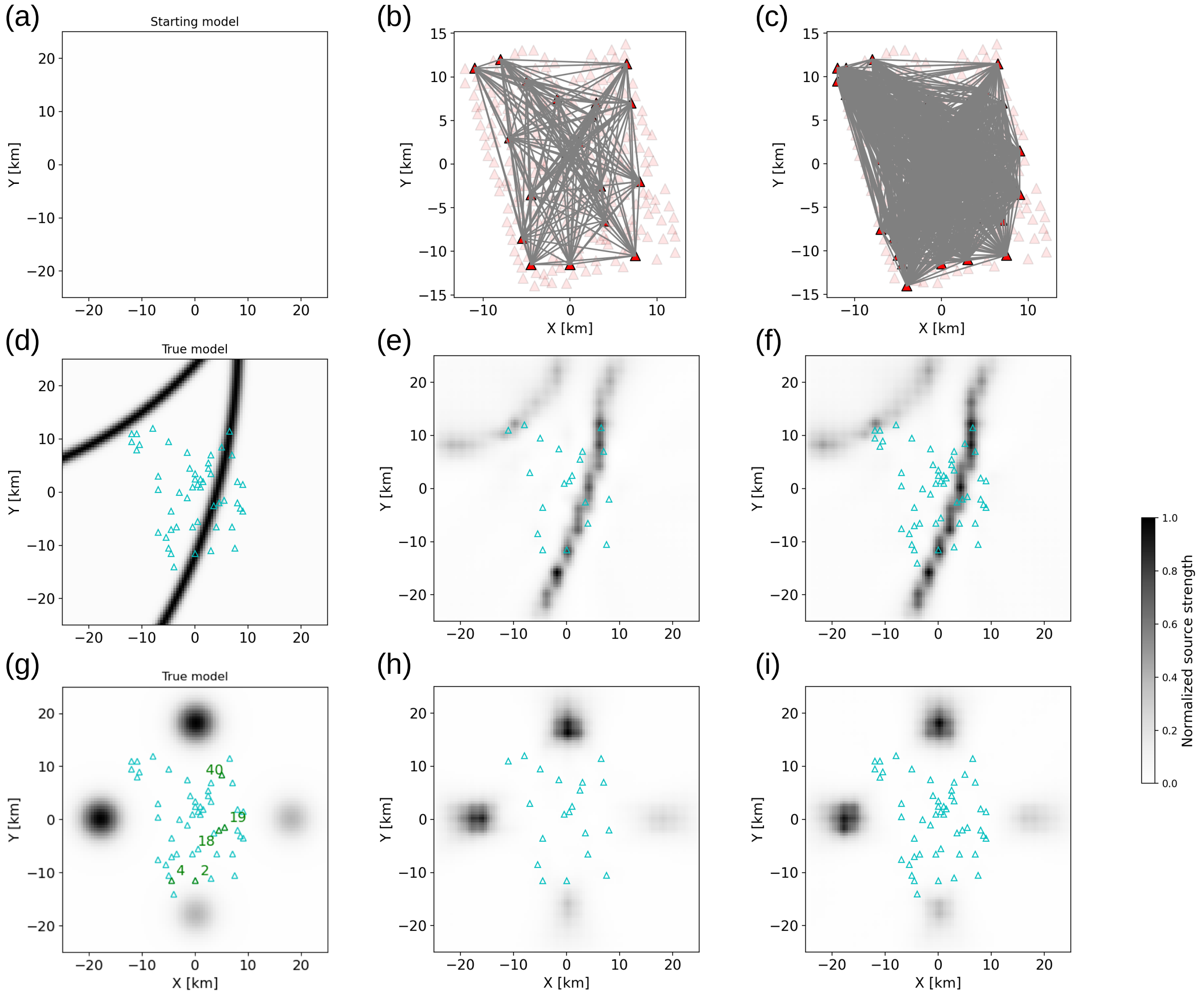

Figure 2. Source inversion results with homogeneous velocity models. (a) Starting model for all inversions – same as Figure 1 but with different normalization as described below. (b)-(c) Tomographic setup used for inversion: map with 20 and 50 receivers selected respectively (red triangles), along with inter-receiver ray paths (grey lines). (d) TSM-1, shown with the 50 receivers selected in (c). (e)-(f) Inversion results for TSM-1, using 20 and 50 receivers respectively. (g) TSM-2, shown with 50 receivers and with a few receivers labelled for association with subsequent figures. (h)-(i) Inversion results for TSM-2, using 20 and 50 receivers respectively. All source distributions are shown normalized by their maximum value (to focus on relative source strength), with the exception of the starting model (a), which is normalized with respect to the test models in order to illustrate its low amplitude.

3.1 Impact of heterogeneous velocity structure

To investigate the effects of heterogeneous structure, we use two types of velocity models:

(i) a single low velocity anomaly (Figure 3) – this is a smooth model containing ‘long wavelength' velocity variations (length scale $\gg \lambda_0$), but with an average velocity lower than 2 km/s. It represents a baseline shift relative to the homogeneous velocity model used in Fig. 2).

(ii) a checkerboard (Figure 4) – here the average velocity is equal to that of the homogeneous model (no baseline shift), but there are 'short-wavelength' velocity variations (length scale $\sim \lambda_0$).

With both velocity models, we consider perturbation amplitudes of 5, 10 and 20% relative to the reference homogeneous velocity of 2 km/s. Test data are generated using these heterogeneous velocity models. Inversions are then performed both with and without knowledge of the accurate velocity models. In this section, we present tests performed with the 50-receiver array geometry only.

When the velocity information provided in inversion is accurate (Fig. 3(d-f)), we obtain results that are all nearly identical to the homogeneous velocity case. The inverse modelling can tolerate errors in velocity information up to 10%, but artefacts appear for the case of 20% velocity heterogeneity (Fig. 3(g-i)). Also, sources outside the array are not retrieved accurately in this case. With the checkerboard velocity model, inversion artefacts, at 20% heterogeneity, are more pronounced (Figure 4), reflecting the complications of wave propagation through short-wavelength structural variations. In Figure 5, we compare a few waveform fits from the long wavelength anomaly model (Fig. 3i) with those from the checkerboard model (Fig. 4i) at 20% velocity perturbation. The long-wavelength anomaly primarily affects the phase of the propagating waves. For receiver pairs separated by large distances (e.g. Fig. 5c), the observed and predicted waveforms are separated by more than half-a-cycle ($\sim$ 2.5 s), leading to poor inversion results: this is the well known phenomenon of cycle skipping (Virieux & Operto 2009). We note that the energy-based misfit function is not immune to cycle skipping, but analysis of misfit functions in this context is beyond the scope of this study. The short-wavelength checkerboard model, on the other hand, produces significant multiple scattering. Scattering is visible in the cross-correlation waveforms (e.g. Fig. 5g), and confirmed through the wavefields u (not shown), which arise from point sources and produce the cross-correlations via equation (2).

Similar tests with the second source model, TSM-2, are presented in Figures 6 and 7. In contrast to TSM-1, TSM-2 is a simpler model and the sources exist only outside the array. All source

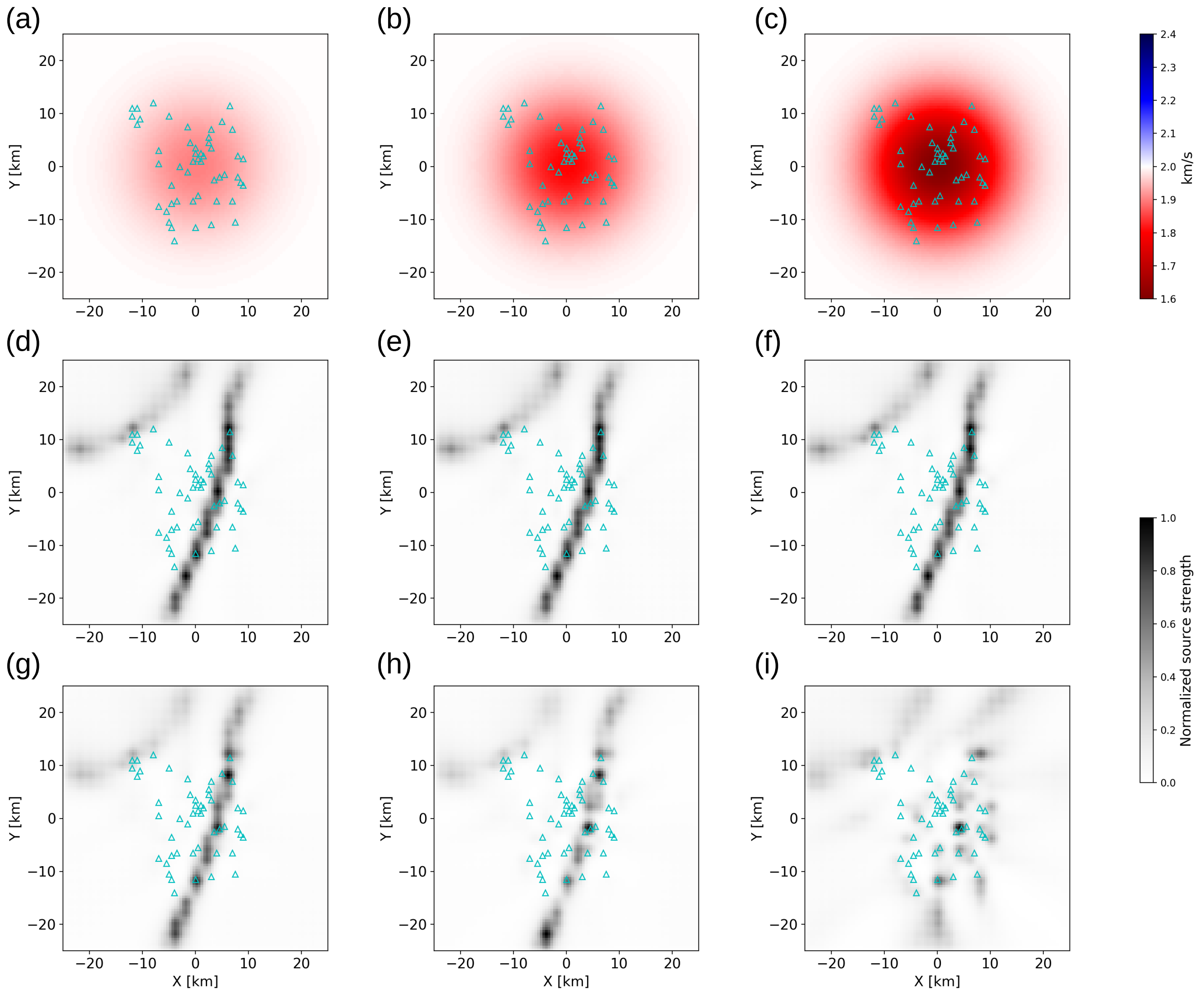

Figure 3. Source inversion results with 2-D velocity models. Top row: Velocity models with a perturbation amplitude of (a) 5% (b) 10% (c) 20%. Middle row: Inversion results for TSM 1, obtained using an accurate velocity model, i.e. velocity models (a)-(c) are used to generate synthetic test data, as well as in source inversion leading to the corresponding results (d)-(f). Bottom row: Results of inversion performed without an accurate velocity model, i.e. velocity models (a)-(c) are used to generate synthetic test data, but source inversion is performed using a homogeneous velocity model. In all cases, the starting (source) model for inversion is the same as in Figure 2a.

regions are reasonably well recovered, for velocity inaccuracies of up to 10%. For the case of unmodelled 20% velocity heterogeneity, the low velocity anomaly produces some distortion of sources, while strong aretefacts appear with the checkerboard velocity model. We also performed tests with a long wavelength checkerboard model and verified that the phase perturbations due to positive and negative anomalies compensate each other, leading to improved inversion results even at 20% velocity perturbation.

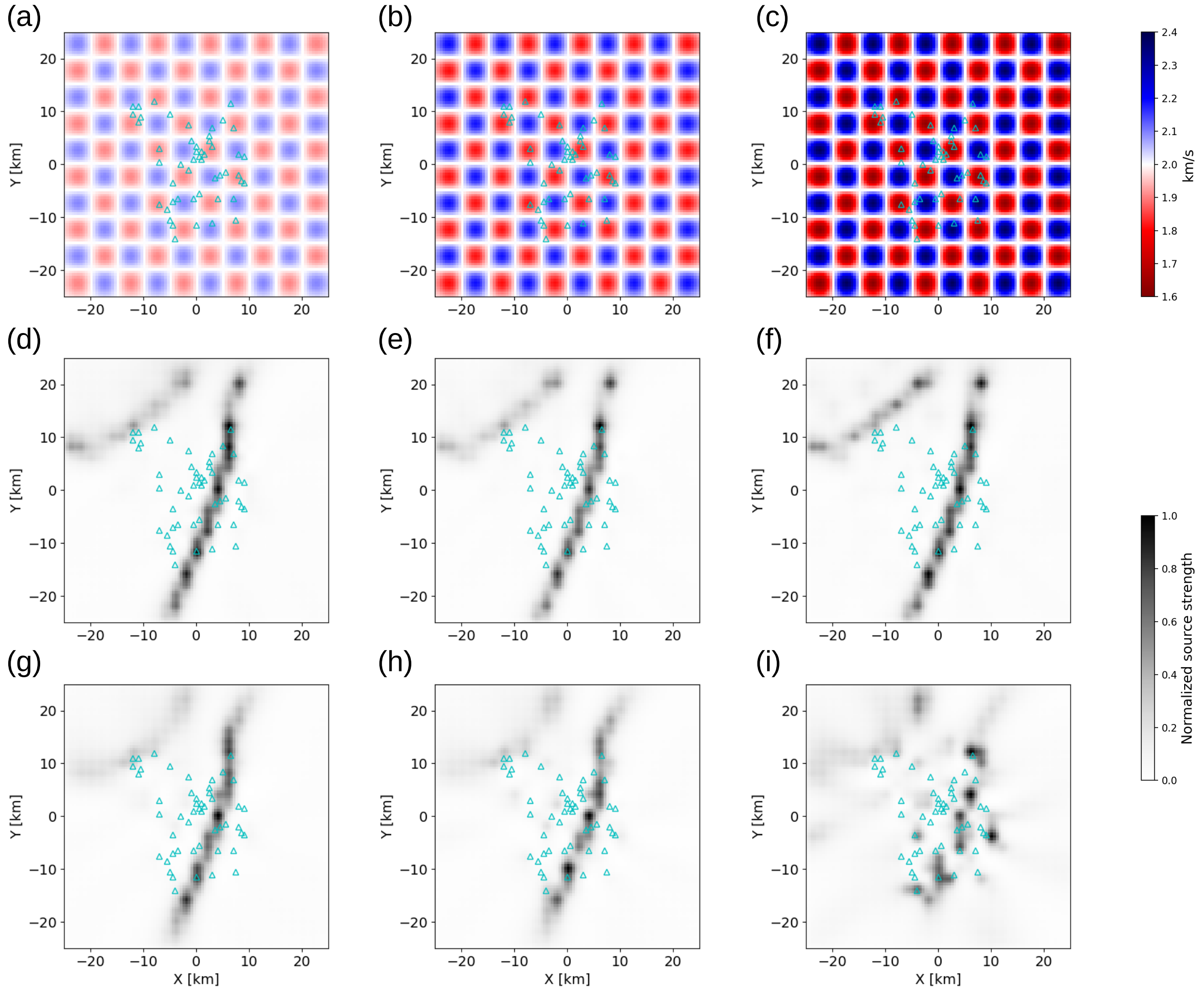

Figure 4. Similar to Figure 3, but using checkerboard-style velocity models.

222 It should be emphasised that the $\sigma(\mathbf{x})$ starting model is the same (see Fig. 2a) for all tests in 223 this section. On the other hand, the optimal value of the damping parameter used in inversion, is 224 determined separately in each case by independent L-curve analysis.

Parameter	Value
Uniform grid spacing	0.5 km
Reference homogeneous wavespeed	2 km/s
Central frequency	0.2 Hz
Time series length	60 s
Temporal sampling (upper bound)	0.1 s
Basis function width (4σ)	5 km
Basis function spacing	2 km

Table 1. Simulation parameters used. Disambiguation: here σ denotes the standard deviation of 2-D Gaussian functions used as model basis.

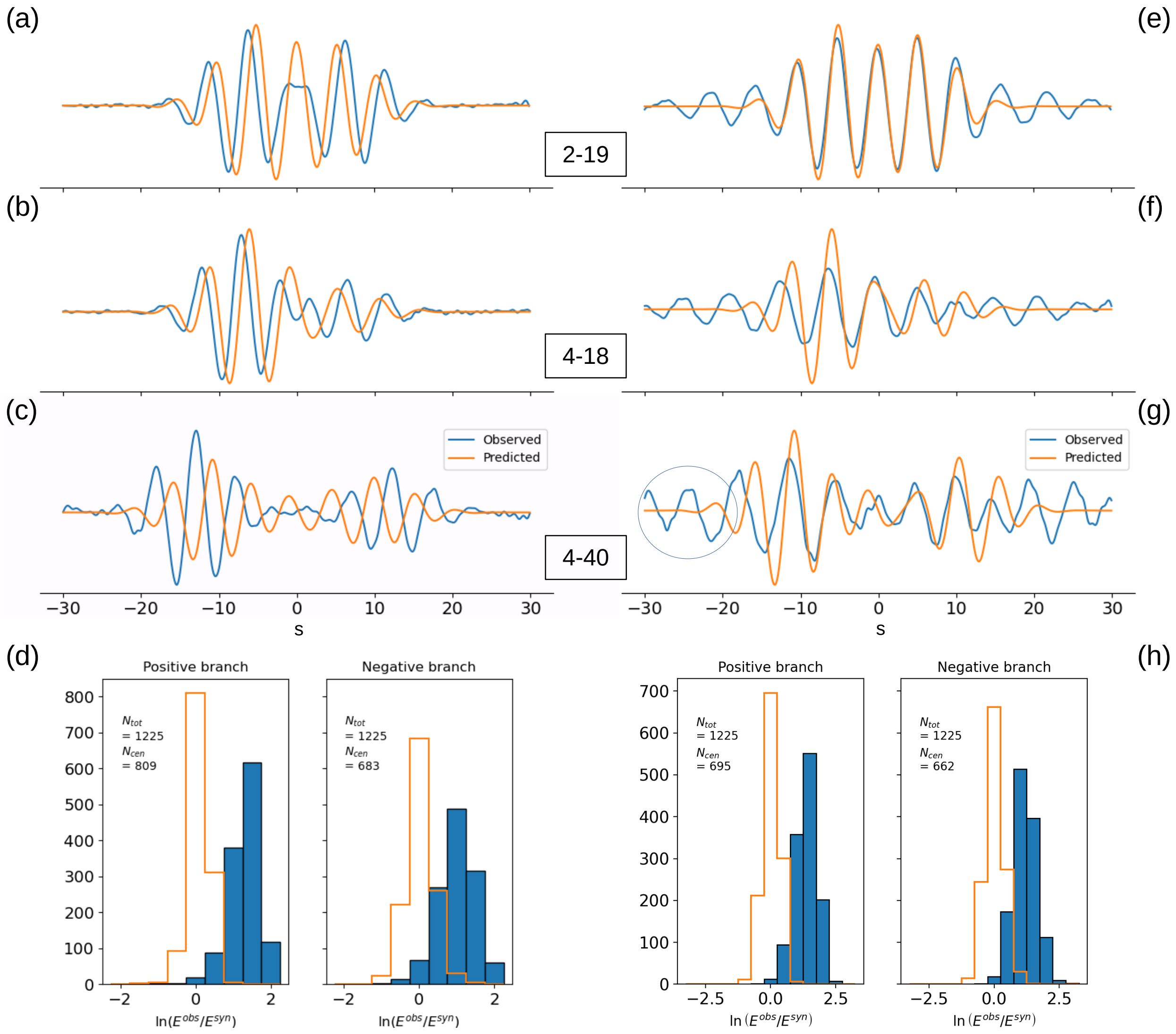

Figure 5. Fit to crosscorrelograms for selected receiver pairs (highlighted in Figure 2g) corresponding to the single low velocity anomaly (a – c) and checkerboard velocity models (e – g), both with a velocity perturbation magnitude of 20%. Cycle skipping is readily apparent in (c). Part of the waveforms are highlighted in (g) to show the effect of scattering. (d), (h) Inversion statistics: after inversion (orange outline bars), no. of measurements in the central histogram bins (fit accuracy at least 72%) is approximately 60% for the single anomaly (d) and 55% for the checkerboard model (h). This refers to all measurements, i.e. positive and negative branches combined. The blue filled bars represent the measurements at the start of the inversion, i.e. for the initial model. For reference, ‘good inversions’, such as plots (d-f) in Figures 3 and 4, put $> 99\%$ of measurements in the central bin of similarly constructed histograms.

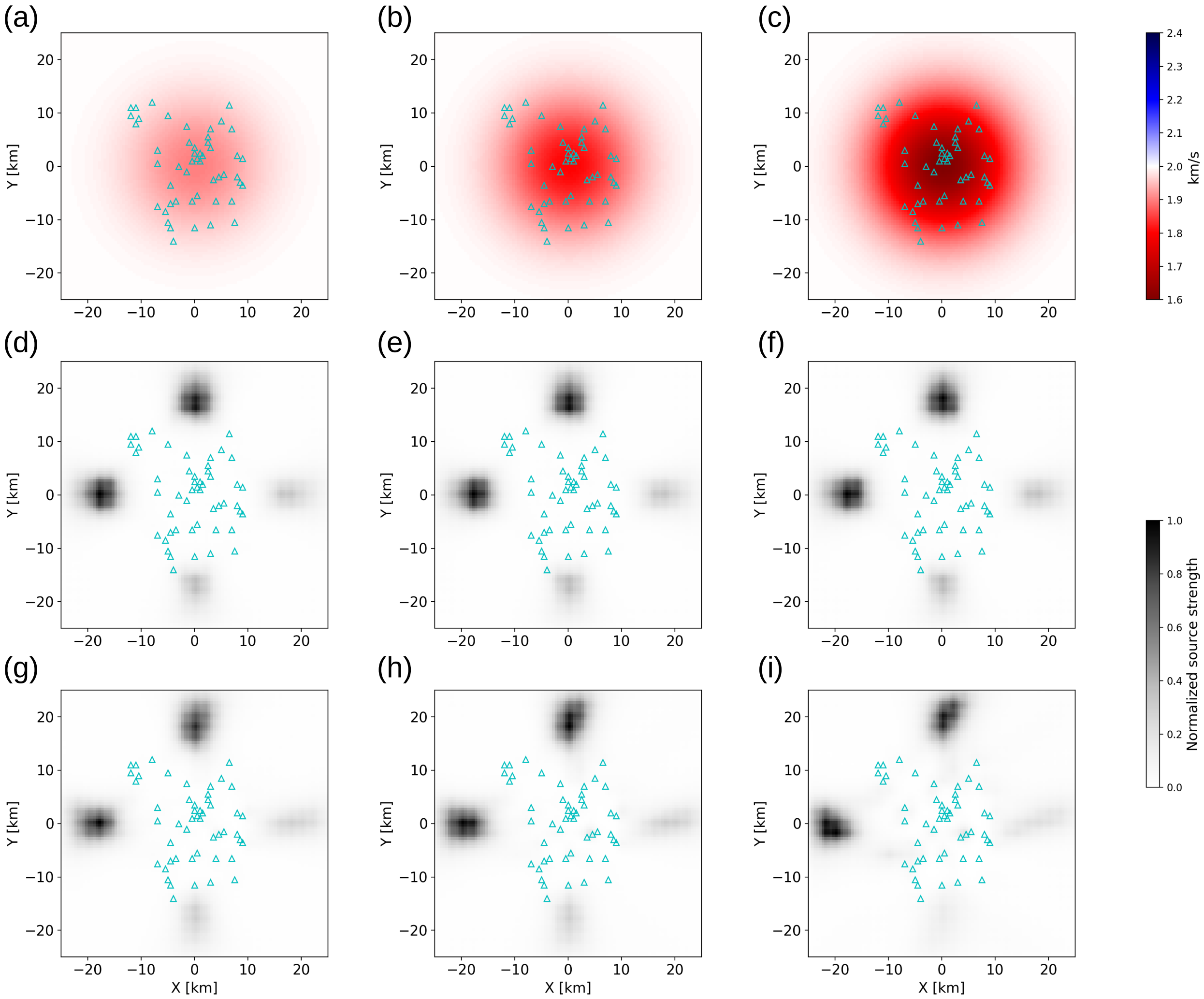

Figure 6. Similar to Figure 3 but for TSM-2.

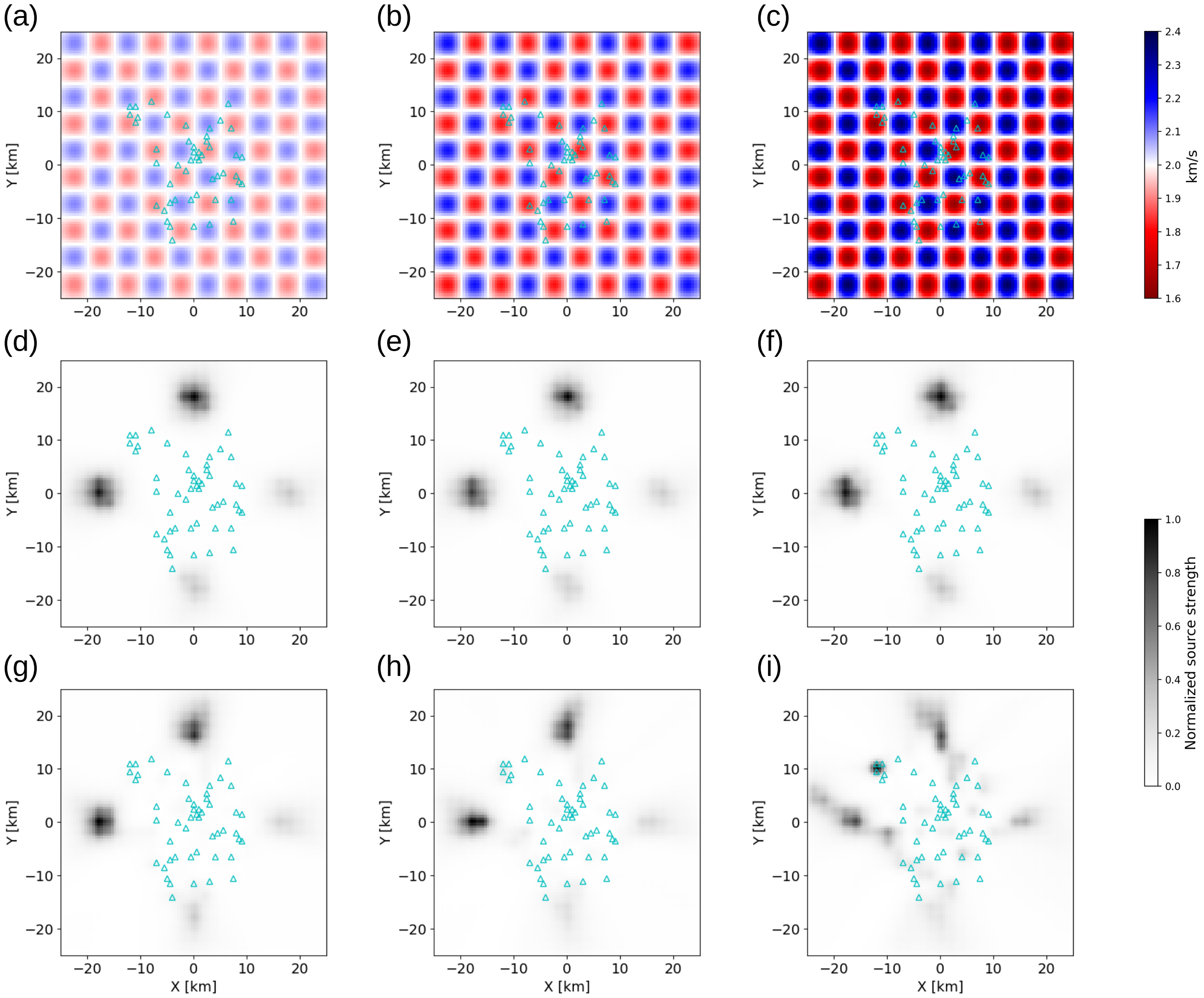

Figure 7. Similar to Figure 4 but for TSM-2.

4 CONCLUSIONS

In this paper, we have considered two contentious issues in the ambient seismic source inversion literature – source resolution outside the sensor array (empirical constraints only), and sensitivity of source inversion to velocity structure heterogeneity. Based on our synthetic tests, we conclude that:

(i) it is possible to accurately recover source distributions up to a certain distance from the sensor array, as long as the forward modelling theory (Section 2.1) is valid.

(ii) accurate modelling of velocity structure, within the acoustic approximation, has limited impact on ambient noise source inversion. Detrimental effects of assuming a simplistic velocity model are seen only when the assumed model is a very poor approximation to the true structure. For media with weak lateral heterogeneity, even the simplest approximation of a homogeneous medium (with a reference wavespeed accurate to within 10%) may be acceptable. It becomes unacceptable when true wavespeed variations exceed 20% of the assumed reference value, due to unmodelled scattering and/or phase distortions. This has a bearing on realistic scenarios where the velocity structure is not known *a priori*. With real data, one can expect unmodelled lateral heterogeneity to have a greater impact on source inversion, because real data would be beset with 'modelling error' (which was absent in the synthetic data of Section 3).

These conclusions are specific to the particular technique used, as elaborated below.

5 DISCUSSION

We have introduced an acoustic full waveform inversion technique for ambient noise source distribution. Although more sophisticated techniques, which account for Earth's three-dimensional, elastic (and anelastic) structure already exist (e.g. Ermert et al. 2017, 2021), our method occupies a niche within the field. Compared to 3-D elastic FWI, it incorporates a significant amount of modelling rigour, at a fraction of the computational cost. Our implementation does not require writing to disk during simulations, and most of our simulations were performed on a desktop computer with 64 GB RAM. A second convenience of our technique is that it can leverage results from the immensely popular field of ray-based ambient noise surface wave tomography. Surface wave group velocity maps produced by ray-based methods (e.g. Shekar et al. 2023) can be used to characterize Earth structure in our source inversion scheme. More generally, such maps can be used as starting structure models in a future joint source-structure acoustic inversion scheme, which may serve to refine traditional ambient noise tomographic models. An obvious limitation of this technique is the acoustic regime, which limits us to membrane wave simulations and precludes the use of any multicomponent information from ambient noise cross-correlations (e.g. Xu & Mikesell 2017; Malkoti et al. 2021).

In the context of the existing literature, we recognize that our conclusions (Section 4) are inextricably linked to the inversion strategy, particularly the choice of the misfit function. This statement arguably also applies to our optimization scheme. We surmise that Hessian-based optimization is at least partly responsible for our success in recovering outside-array sources, compared to Xu et al. (2019), who used a purely gradient-based optimization. We note that approximate Hessian information, via the L-BFGS algorithm, was also used by Ermert et al. (2020) and Sager et al. (2018b). Indeed, the inverse of the approximate Hessian can act as a focusing operator that compensates for uneven illumination and finite bandwidth of the wavefields (Pratt et al. 1998).

Application of our technique to real data is a subject of ongoing research. In the future, its technical scope can be widened in several ways. For example, the assumption of uniform spectral character of all ambient sources can be relaxed to invert for space- as well as frequency- dependent ambient source distribution (e.g. Ermert et al. 2017, 2021). While this considerably expands the parameter space, techniques like sparsity promotion (e.g. Shekar & Sethi 2019) can be employed to constrain the inversion. Another line of development would be to extend to 3-D elastic modelling, and we note that this is possible with the “Devito” package itself.

ACKNOWLEDGEMENTS

This research is supported by the Department of Science and Technology, Government of India, via an INSPIRE Faculty grant to AD. PLK gratefully acknowledges support from this grant while at IISER Pune. The support and resources provided by the Param Brahma HPC facility under the National Supercomputing Mission, Government of India, at IISER Pune are gratefully acknowledged, as it was used to perform some of the simulations in this study. We thank reviewers Laura Ermert and Jonas Igel for their constructive feedback which greatly helped to improve this manuscript.

Data availability

No new data were generated or analysed in support of this research. The source inversion code used in this work is available on github: https://github.com/ arjundatta23/cc_kern_inv.

REFERENCES

Aso, N., Tsai, V. C., Schoof, C., Flowers, G. E., Whiteford, A., & Rada, C., 2017. Seismologically observed spatiotemporal drainage activity at moulins, *Journal of Geophysical Research: Solid Earth*, **122**, 9095–9108.

Bensen, G. D., Ritzwoller, M. H., Barmin, M. P., Levshin, A. L., Lin, F., Moschetti, M. P., Shapiro, N. M., & Yang, Y., 2007. Processing seismic ambient noise data to obtain reliable broad-band surface wave dispersion measurements, *Geophysical Journal International*, **169**, 1239–1260.

Cros, E., Roux, P., Vandemeulebrouck, J., & Kedar, S., 2011. Locating hydrothermal acoustic sources at old faithful geyser using matched field processing, *Geophysical Journal International*, **187**, 385–393.

Dahlen, F. A., Hung, S.-H., & Nolet, G., 2000. Fréchet kernels for finite-frequency traveltimes-i. theory, *Geophysical Journal International*, **141**, 157–174.

Datta, A., Hanasoge, S., & Goudswaard, J., 2019. Finite frequency inversion of cross-correlation amplitudes for ambient noise source directivity estimation, *Journal of Geophysical Research: Solid Earth*, **124**, 6653–6665.

Ermert, L., Villaseñor, A., & Fichtner, A., 2016. Cross-correlation imaging of ambient noise sources, *Geophysical Journal International*, **204**, 347–364.

Ermert, L., Sager, K., Afanasiev, M., Boehm, C., & Fichtner, A., 2017. Ambient seismic source inversion in a heterogeneous earth: Theory and application to the earth's hum, *Journal of Geophysical Research: Solid Earth*, **122**, 9184–9207.

Ermert, L., Igel, J., Sager, K., Stutzmann, E., Nissen-Meyer, T., & Fichtner, A., 2020. Introducing noisi: A python tool for ambient noise cross-correlation modeling and noise source inversion, *Solid Earth*, **11**, 1597–1615.

Ermert, L. A., Sager, K., Nissen-Meyer, T., & Fichtner, A., 2021. Multifrequency inversion of global ambient seismic sources, *Geophysical Journal International*, **225**, 1616–1623.

Fichtner, A., 2014. Source and processing effects on noise correlations, *Geophysical Journal International*, **197**, 1527–1531.

Fichtner, A., Stehly, L., Ermert, L., & Boehm, C., 2017. Generalized interferometry – i: theory for interstation correlations, *Geophysical Journal International*, **208**, 603–638.

Gal, M., Reading, A. M., Ellingsen, S. P., Gualtieri, L., Koper, K. D., Burlacu, R., Tkalčiïc, H., & Hemer, M. A., 2015. The frequency dependence and locations of short-period microseisms generated in the southern ocean and west pacific, *Journal of Geophysical Research: Solid Earth*, **120**, 5764–5781.

Gerstoft, P. & Tanimoto, T., 2007. A year of microseisms in southern california, *Geophysical Research Letters*, **34**, L20304.

Hanasoge, S. M., 2013. The influence of noise sources on cross-correlation amplitudes, *Geophysical Journal International*, **192**, 295–309.

Hanasoge, S. M., 2014. Measurements and kernels for source-structure inversions in noise tomography, *Geophysical Journal International Geophys. J. Int*, **196**, 971–985.

Hansen, P. C. & O'Leary, D. P., 1993. The use of the l-curve in the regularization of discrete ill-posed problems, *Siam Journal on Scientific Computing*, **14**, 1487–1503.

Igel, J. K., Ermert, L. A., & Fichtner, A., 2021. Rapid finite-frequency microseismic noise source inversion at regional to global scales, *Geophysical Journal International*, **227**, 169–183.

Juretzek, C. & Hadziioannou, C., 2016. Where do ocean microseisms come from? a study of love-to-rayleigh wave ratios, *Journal of Geophysical Research: Solid Earth*, **121**, 6741–6756.

Kimman, W. P. & Trampert, J., 2010. Approximations in seismic interferometry and their effects on surface waves, *Geophysical Journal International*, **182**, 461–476.

Kumar, N., Shekar, B., & Singh, S., 2022. A nodal integral scheme for acoustic wavefield simulation, *Pure and Applied Geophysics*, **179**, 3677–3691.

Labedz, C. R., Bartholomaus, T. C., Amundson, J. M., Gimbert, F., Karplus, M. S., Tsai, V. C., & Veitch, S. A., 2022. Seismic mapping of subglacial hydrology reveals previously undetected pressurization event, *Journal of Geophysical Research: Earth Surface*, p. e2021JF006406.

Liu, Q., Koper, K. D., Burlacu, R., Ni, S., Wang, F., Zou, C., Wei, Y., Gal, M., & Reading, A. M., 2016. Source locations of teleseismic p, sv, and sh waves observed in microseisms recorded by a large aperture seismic array in china, *Earth and Planetary Science Letters*.

Louboutin, M., Lange, M., Luporini, F., Kukreja, N., Witte, P. A., Herrmann, F. J., Velesko, P., & Gorman, G. J., 2019. Devito (v3.1.0): an embedded domain-specific language for finite differences and geophysical exploration, *Geoscientific Model Development*, **12**(3), 1165–1187.

Luporini, F., Louboutin, M., Lange, M., Kukreja, N., Witte, P., Hückelheim, J., Yount, C., Kelly, P. H. J., Herrmann, F. J., & Gorman, G. J., 2020. Architecture and performance of devito, a system for automated stencil computation, *ACM Trans. Math. Softw.*, **46**(1).

Malkoti, A., Datta, A., & Hanasoge, S. M., 2021. Rayleigh-wave h/v ratio measurement from ambient noise cross-correlations and its sensitivity to vp: a numerical study, *Geophysical Journal International*, **227**, 472–482.

Meurer, A., Smith, C. P., Paprocki, M., Čertík, O., Kirpichev, S. B., Rocklin, M., Kumar, A., Ivanov, S., Moore, J. K., Singh, S., Rathnayake, T., Vig, S., Granger, B. E., Muller, R. P., Bonazzi, F., Gupta, H., Vats, S., Johansson, F., Pedregosa, F., Curry, M. J., Terrel, A. R., Roučka, v., Saboo, A., Fernando, I., Kulal, S., Cimrman, R., & Scopatz, A., 2017. Sympy: symbolic computing in python, *PeerJ Computer Science*, **3**, e103.

Pratt, R. G., Shin, C., & Hick, G. J., 1998. Gauss–newton and full newton methods in frequency–space seismic waveform inversion, *Geophys. J. Int.*, **133**, 341–362.

Retailleau, L. & Gualtieri, L., 2019. Toward high-resolution period-dependent seismic monitoring of tropical cyclones, *Geophysical Research Letters*, **46**, 1329–1337.

Roux, P., Sabra, K. G., Kuperman, W. A., & Roux, A., 2005. Ambient noise cross correlation in free space: Theoretical approach, *The Journal of the Acoustical Society of America*, **117**, 79–84.

Sager, K., Boehm, C., Ermert, L., Krischer, L., & Fichtner, A., 2018a. Sensitivity of seismic noise correlation functions to global noise sources, *Journal of Geophysical Research: Solid Earth*.

Sager, K., Ermert, L., Boehm, C., & Fichtner, A., 2018b. Towards full waveform ambient noise inversion, *Geophysical Journal International*, **212**, 566–590.

Sager, K., Boehm, C., Ermert, L., Krischer, L., & Fichtner, A., 2020. Global-scale full-waveform ambient noise inversion, *Journal of Geophysical Research: Solid Earth*, **125**, e2019JB018644.

Shapiro, N. M., 2019. Applications with surface waves extracted from ambient seismic noise, in *Seismic Ambient Noise*, pp. 218–238, eds Nakata, N., Gualtieri, L., & Fichtner, A., Cambridge Univ. Press.

Shapiro, N. M. & Campillo, M., 2004. Emergence of broadband rayleigh waves from correlations of the ambient seismic noise, *Geophysical Research Letters*, **31**, n/a–n/a.

Shekar, B. & Sethi, H. S., 2019. Full-waveform inversion for microseismic events using sparsity constraints, *Geophysics*, **84**(2), KS1–KS12.

Shekar, B., Mohan, G., & Singh, S. K., 2023. Structural information derived from ambient noise tomography over a hydrocarbon producing region in cachar fold belt, lower assam, northeast india, *Geophysical Prospecting*, **71**(1), 140–162.

Snieder, R., 2004. Extracting the green's function from the correlation of coda waves: A derivation based on stationary phase, *Physical Review E*, **69**, 046610.

Tian, Y. & Ritzwoller, M. H., 2015. Directionality of ambient noise on the juan de fuca plate: implications for source locations of the primary and secondary microseisms, *Geophysical Journal International*, **201**, 429–443.

Tromp, J., Tape, C., & Liu, Q., 2005. Seismic tomography, adjoint methods, time reversal and banana-doughnut kernels, *Geophysical Journal International*, **160**, 195–216.

Tromp, J., Luo, Y., Hanasoge, S., & Peter, D., 2010. Noise cross-correlation sensitivity kernels, *Geophysical Journal International*, **183**, 791–819.

Tsai, V. C., Minchew, B., Lamb, M. P., & Ampuero, J. P., 2012. A physical model for seismic noise generation from sediment transport in rivers, *Geophysical Research Letters*, **39**, 2404.

Virieux, J. & Operto, S., 2009. An overview of full-waveform inversion in exploration geophysics, *Geophysics*, **74**(6), WCC1–WCC26.

Xu, Z. & Mikesell, T. D., 2017. On the reliability of direct rayleigh-wave estimation from multicomponent cross-correlations, *Geophysical Journal International*, **210**, 1388–1393.

Xu, Z. & Mikesell, T. D., 2022. Estimation of resolution and covariance of ambient seismic source distributions: Full waveform inversion and matched field processing, *Journal of Geophysical Research: Solid Earth*, **127**, e2022JB024374.

Xu, Z., Mikesell, T. D., Gribler, G., & Mordret, A., 2019. Rayleigh-wave multicomponent cross-correlation-based source strength distribution inversion. part 1: Theory and numerical examples, *Geophysical Journal International*, **218**, 1761–1780.

Xu, Z., Mikesell, T. D., Umlauft, J., & Gribler, G., 2020. Rayleigh-wave multicomponent crosscorrelation-based source strength distribution inversions. part 2: a workflow for field seismic data, *Geophysical Journal International*, **222**, 2084–2101.

Yao, H. & van der Hilst, R. D., 2009. Analysis of ambient noise energy distribution and phase velocity bias in ambient noise tomography, with application to se tibet, *Geophysical Journal International*, **179**, 1113–1132.

Zhou, C., Xia, J., Cheng, F., Pang, J., Chen, X., Xing, H., & Chang, X., 2022. Passive surface-wave waveform inversion for source-velocity joint imaging, *Surveys in Geophysics*, **43**, 853–881.

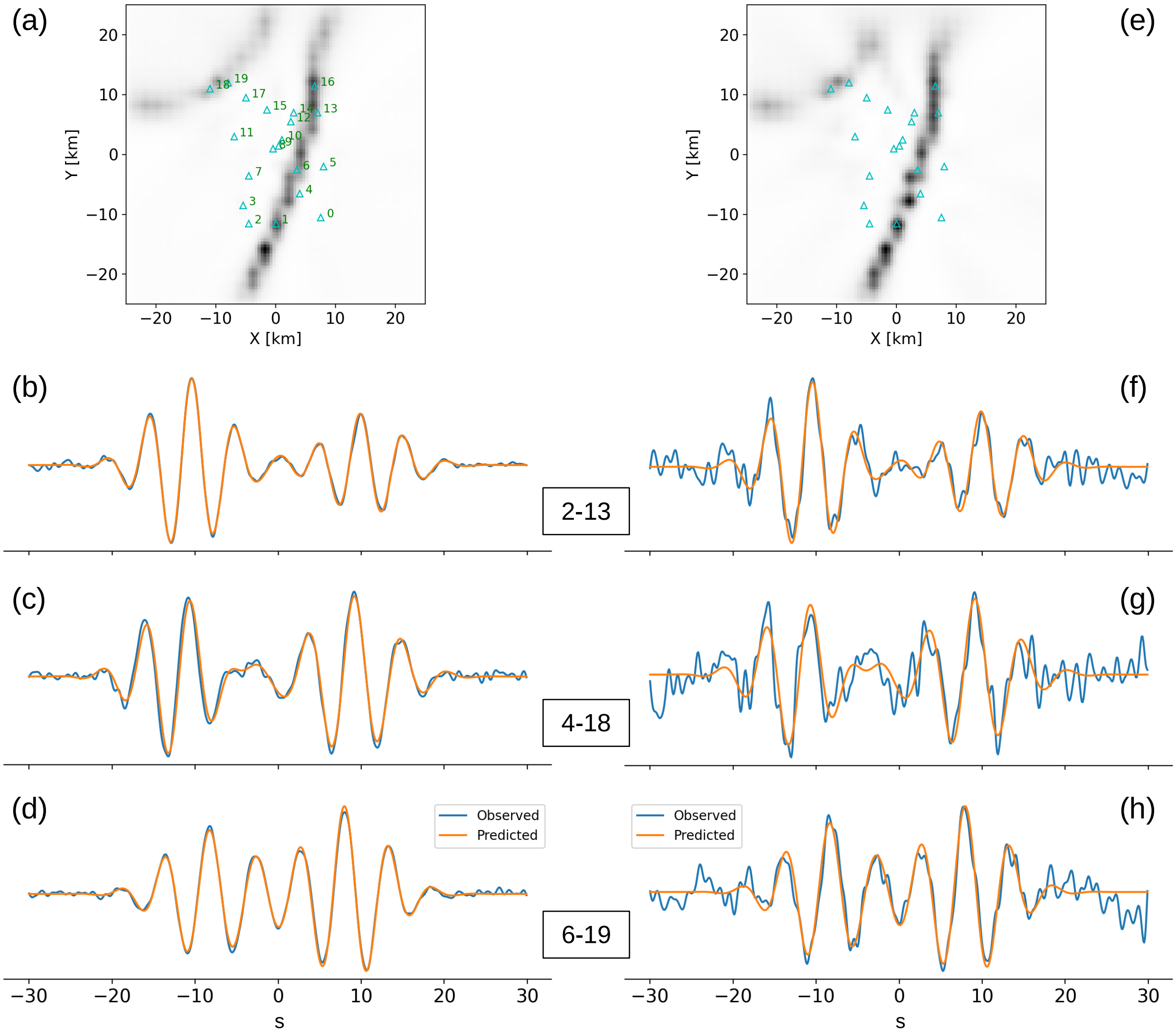

Figure A1. Inversion for TSM-1 with 10% (a-d) and 50% (e-h) noise added to the synthetically generated data. The inversion result is shown at the top, followed by examples of cross-correlation waveform fits for three receiver pairs, as identified by the receiver numbers in boxes. For example, (b), (f) show waveform fits for the pair of receivers numbered 2 and 13. Note that the 10% case corresponds to Figure 2, and (a) is the same as Figure 2(e), but with receiver numbers marked for reference.

APPENDIX A: EFFECT OF NOISY DATA

Figures A1 and A2 compare the inversions of Figure 2 (20 receivers only), with those of more noisy data. Results obtained with only one realization of noise are presented. We note that, at the higher noise level, inversion results can change with different realizations of Gaussian noise.

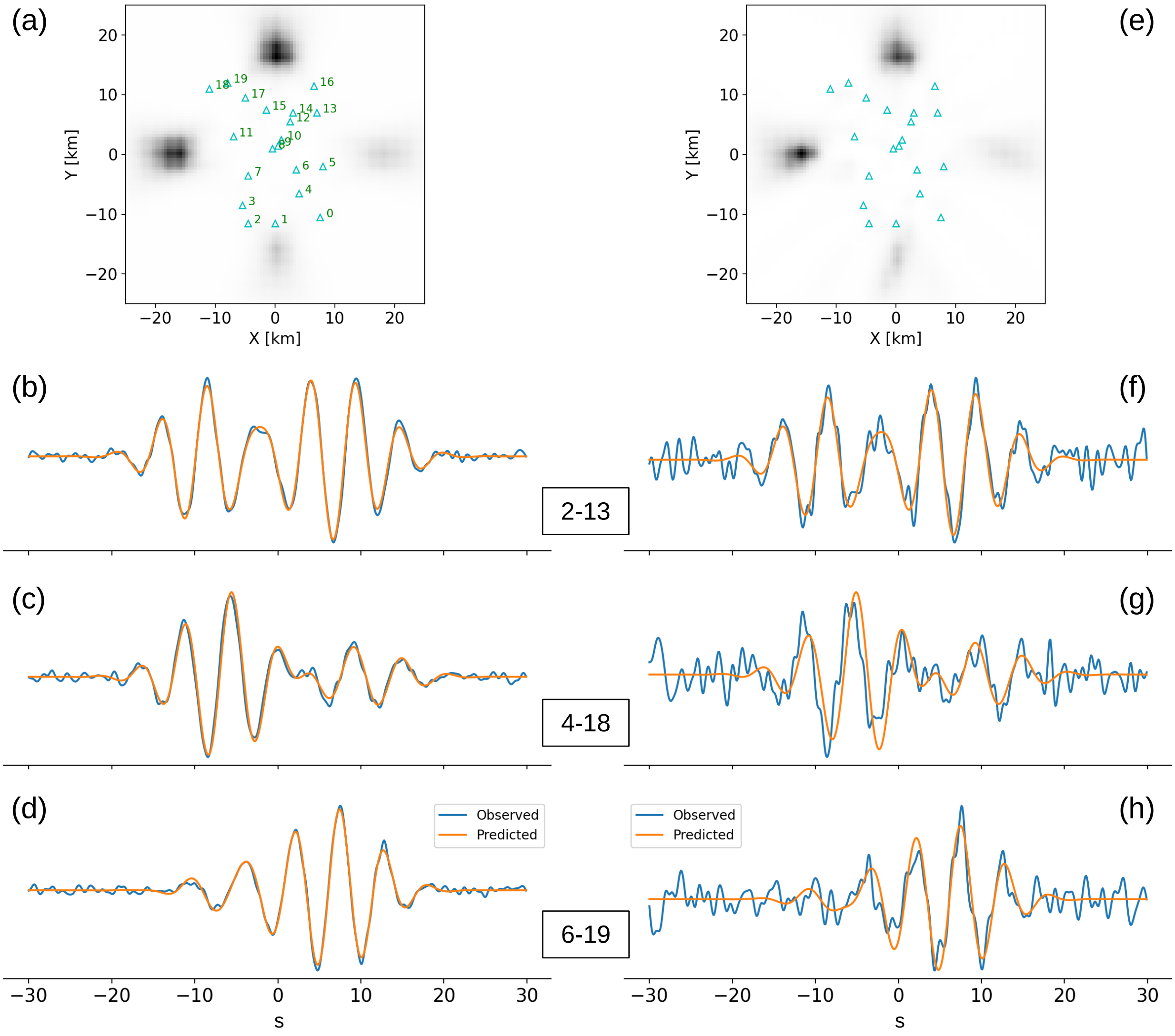

Figure A2. Same as Figure A1, but for TSM-2.

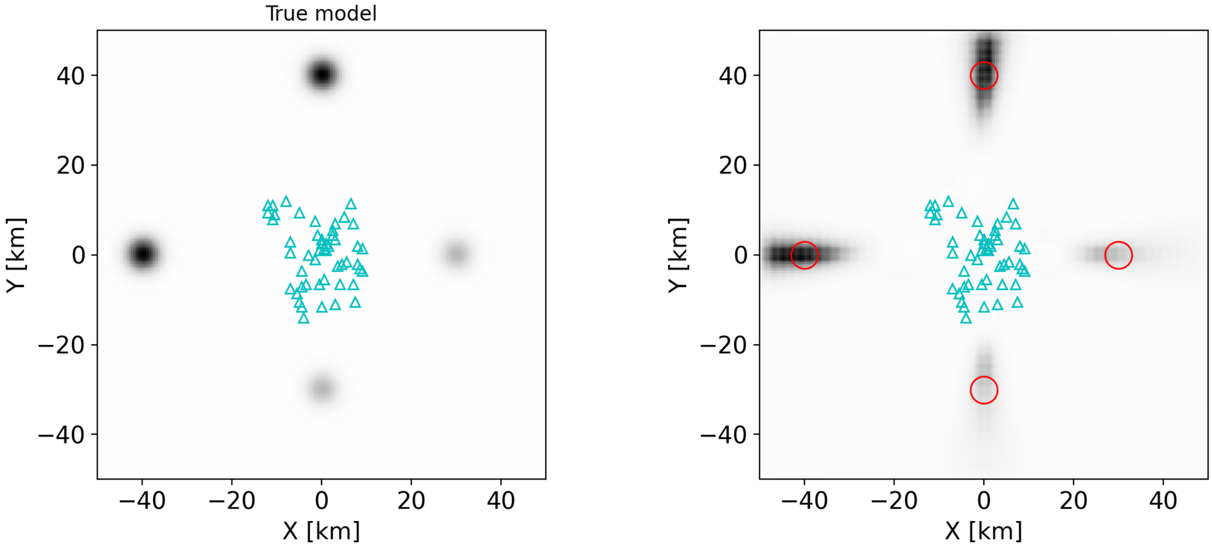

Figure A3. Left: Test model similar to TSM-2, but with the strong and weak source regions placed at distances of 40 km and 30 km respectively, from the array centre. Right: Inversion result for this test model, with open circles marking the true source locations for reference.

406 APPENDIX B: EFFECT OF DISTANCE

407 Figure A3 presents a synthetic test similar to those of Figure 2 (50 receivers only), but using a
408 modelling domain of size 100×100 km.